Carbon nanotube EUV pellicle tunability and performance in a scanner-like environment

Marina Y. Timmermans,* Ivan Pollentier, Maxim Korytov, Thomas Nuytten, Stefanie Sergeant, Thierry Conard, Johan Meersschaut, Yide Zhang, Masoud Dialameh, Wilfried Alaerts, Ehsan Jazaeri, Valentina Spampinato, Alexis Franquet, Steven Brems, Cedric Huyghebaert, and Emily E. Gallagher
IMEC, Leuven, Belgium

Abstract

Background: An extreme ultraviolet (EUV)-transparent pellicle must be used during lithography to protect the photomask from fall-on particles. A pellicle made of free-standing carbon nanotube (CNT) films stops particles despite the presence of gaps while demonstrating high EUV transmission, mechanical stability, low EUV scattering and reflectivity, and DUV transmission that enables through-pellicle mask inspection.

Aim: The CNT EUV pellicle properties can be tailored based on the diversity of CNT structures and tunability of their configuration within the CNT film (density, bundle size, composition, etc.) as shown in this work. A remaining challenge is extending the CNT EUV pellicle lifetime in the scanner environment of EUV-induced hydrogen-based plasma, and the effects on different CNT films are explored here.

Approach: Optical and thermal properties of different CNT pellicles with respect to the CNT material type, density, composition, and bundle size were explored. The ability of uncoated CNT EUV pellicles to withstand high EUV powers in the hydrogen-based environment was tested. Transmission, spectroscopic, and chemical mapping of the exposed CNT membranes were performed to explore the material modifications under various exposure conditions.

Results: Uncoated CNT pellicles withstand 600-W source power equivalent in the EUV scanner-like gas environment but exhibit structural changes with prolonged exposure. Multiwalled CNT pellicles exhibit less EUV transmission change as compared to single-walled CNT pellicles under the same exposure conditions. The protection of CNT material from structural degradation by means of coating was shown.

Conclusions: These investigations add to the understanding of CNT EUV pellicle tunability for optimal performance and lifetime limiters of CNT pellicles under the influence of EUV radiation and plasma. We anticipate the need for coating the CNT pellicle to protect the CNT material against plasma damage for the current scanner conditions. Optimization of both the CNT membrane and its coating is in progress.

 [DOI: 10.1117/1.JMM.20.3.031010]

Keywords: EUV pellicle; carbon nanotubes; free-standing film; tunability; EUV lithography; lifetime; stability; hydrogen plasma; coating.

Paper 21021SS received Mar. 15, 2021; accepted for publication Jun. 30, 2021; published online Jul. 27, 2021.

1 Introduction

Due to its remarkable thermal, electronic, and mechanical properties, carbon nanotube (CNT) material offers a wide range of unique application opportunities. We identified the potential of CNTs to contribute to high yield extreme ultraviolet (EUV) lithography, enabling advanced chip

*Address all correspondence to Marina Y. Timmermans, marina.timmermans@imec.be

1932-5150/2021/$28.00 © 2021 SPIE

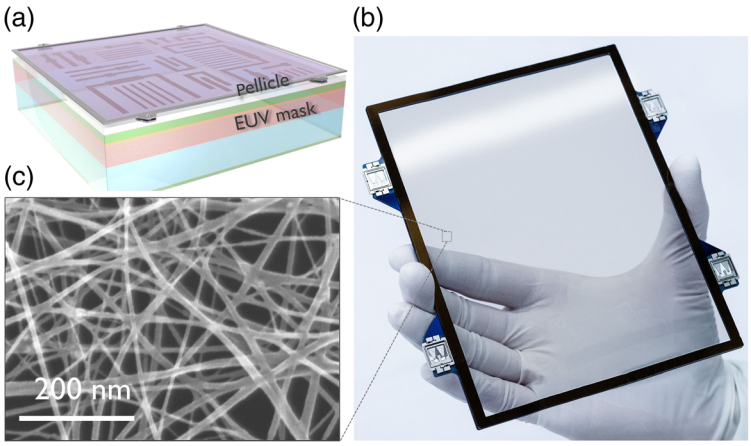

Fig. 1 (a) Schematic representation of an EUV mask with pellicle. Image courtesy of KLA Corp. (b) Photo of a full-size CNT EUV pellicle. (c) SEM image of a random CNT network comprising the pellicle membrane.

manufacturing.[1,2] One of the obstacles in the development of EUV lithography in high volume manufacturing is mask contamination.[3] A pellicle is placed at a few millimeters stand-off distance from the EUV mask so to catch any fall-on particles and not image them onto the wafer by keeping them out of focus. The development of an EUV pellicle to protect the mask is challenging since most of the materials absorb strongly at the 13.5-nm EUV exposure wavelength. To be commercially viable, an EUV pellicle must be thin enough to allow more than 90% EUV light transmittance (EUVT) while durable enough to withstand handling, pressure changes, and thermal stresses. A pellicle made of free-standing CNT films is able to stop particles despite the presence of gaps while demonstrating superior EUVT, mechanical stability, suitable EUV uniformity, low EUV scattering and reflectivity, and sufficient light transmission to allow through-pellicle mask inspection.[1,2,4,5] Figure 1 shows a full-size CNT pellicle ($\sim$110 mm $\times$ 140 mm) similar to one that was successfully exposed on an NXE:3300 EUV scanner at IMEC.[6] Although the concept of using CNTs for the EUV pellicle has demonstrated promise, balancing the CNT material properties for optimal pellicle performance in EUV scanners remains an ongoing research focus.[7,8] Depending on the density and morphology of the CNTs within the film and individual CNT parameters, such as number of walls, bundle size, purity etc., the optical and thermal properties of the CNT pellicle can be tuned. One of the challenges for the EUV pellicle is its stability in the EUV scanner environment, which includes hydrogen plasma and high heat loads associated with EUV exposure at high powers. The study of the CNT material modifications in a scanner-like environment is important to understand the CNT pellicle lifetime.

2 Tailoring the CNT Pellicle Properties

2.1 *CNT Pellicle Fabrication*

A CNT EUV pellicle is made of CNTs randomly intertwined with each other to form a free-standing network structure, which is supported by the pellicle border on the outer edges. A CNT is a hollow, seamless cylinder consisting of a rolled-up sheet of single-layer carbon atoms (graphene). It may be composed of a single graphene layer forming a single-walled CNT (SWCNT), two layers – double-walled CNT (DWCNT), or several graphene sheets rolled up into concentric cylinders – multi-walled CNT (MWCNT). The diameter of individual SWCNTs can be varied from 0.7 to 2 nm, whereas MWCNTs are larger with the diameter up to 100 nm depending on the number of walls. Figure 2 shows the scanning electron micrograph (SEM) example images of pellicles composed of SWCNTs, DWCNTs, and MWCNTs used for the EUV pellicle in this work.

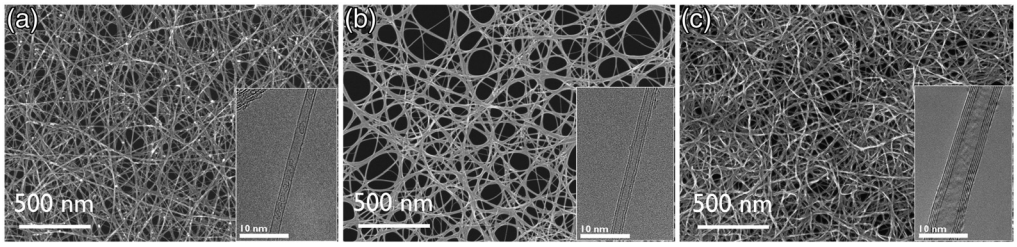

Fig. 2 SEM images of CNT pellicle membrane structure made of (a) SWCNTs, (b) DWCNTs, and (c) MWCNTs. Inset: TEM images of the corresponding CNT types.

The fabrication of a transparent and uniform free-standing CNT film on a support border of a full pellicle size (~110 mm × 140 mm) is not trivial. In this work, free-standing CNT films were produced via two approaches: dry transfer or harvesting from solution. The dry transfer approach utilized a floating catalyst (aerosol) chemical vapor deposition (CVD) method to synthesize CNTs that were then collected onto a filter in a random network and dry-transferred onto a border.[9] In the solvent approach, CNTs were dispersed in liquid, such as water with an addition of surfactant, and deposited onto a filter via vacuum filtration. The CNT film is floated off the filtration membrane and then harvested from the solution onto a support border to create a free-standing membrane.[10] In this work, SWCNT pellicles were fabricated using the dry transfer approach and MWCNT pellicles were harvested from solution. In the past, aligned MWCNT films fabricated by pulling CNT sheets from vertically oriented CNT arrays grown by fixed catalyst CVD method were also explored.[1] This approach was terminated due to the high EUV scattering, nonuniformity, and anisotropic optical properties of such pellicle membranes.[7] In this work, we focus on random configuration of CNTs within the pellicle membrane.

2.2 *EUV Transmittance with Respect to CNT Type and Density*

All types of CNT pellicles, i.e., SWCNT-, DWCNT-, and MWCNT-based, can achieve very high EUVT with acceptable uniformity while remaining mechanically strong. Examples of different CNT EUV pellicles with a corresponding EUVT above the 90%, which is set as the minimum target, and EUVT nonuniformity below 0.4% are shown in Fig. 3. The nonuniformity values are

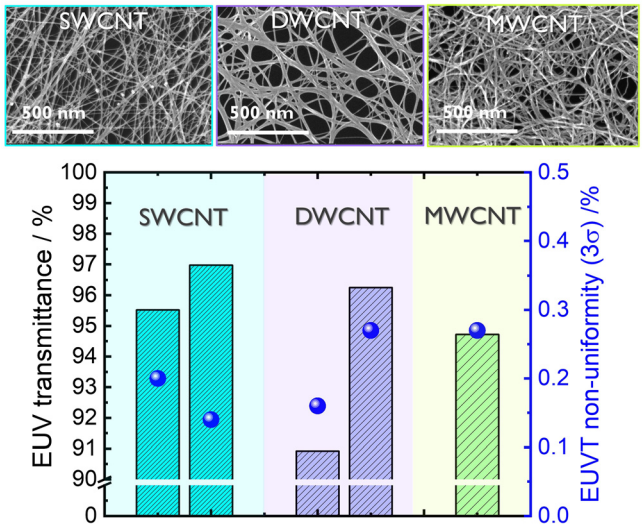

Fig. 3 EUV transmittance (single pass) and EUV transmittance (EUVT) nonuniformity of CNT pellicles made of SWCNTs, DWCNTs, and MWCNTs with the corresponding SEM images of the CNT network. Columns represent EUV transmittance and dots EUVT nonuniformity. EUVT nonuniformity is calculated based on the scanner relevant area of 330 × 330 μm^2 (21 × 21 pixel average).

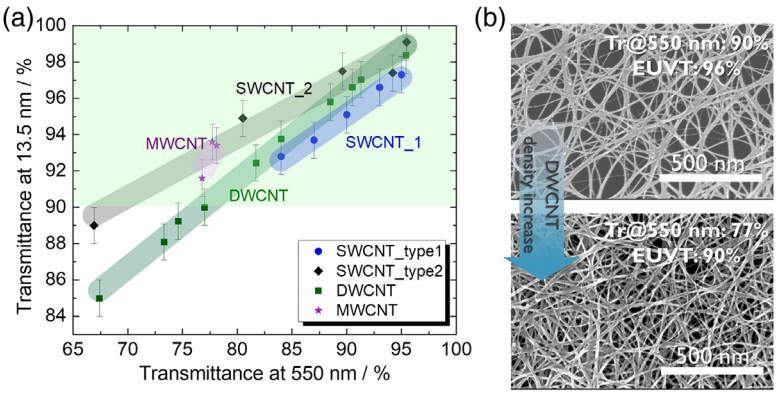

Fig. 4 (a) Correlation between the transmittance at 13.5 and 550 nm for different CNT types. SWCNT_type1 and SWCNT_type2 are pellicles synthesized with different process conditions and differ in composition and film microstructure. (b) SEM images demonstrating an example of CNT density variation for a DWCNT pellicle.

calculated based on the EUVT maps using the scanner relevant area of $330 \times 330\ \mu m^2$, which originates from the EUV light spot size on a pellicle that is held out of the focal plane during a scanner exposure. Although the interaction of EUV light on the nanoscale level of individual CNTs will be polarization dependent (a cylinder-like structure will pass light differently, depending on the polarization orientation to the cylinder orientation), the random configuration of the large quantity of CNTs within the pellicle will spread the polarization effects. Therefore, we anticipate the CNT pellicle to exhibit quasi-isotropic optical properties, and hence also no significant impact on imaging is expected.

The EUVT of a CNT pellicle can be tuned by varying the density or the amount of CNTs within the membrane. Depending on the fabrication approach, the CNT areal density can be adjusted by either varying the CNT collection time during the floating catalyst CVD synthesis or by modifying the amount of CNT material collected during vacuum filtration from the solution. Spectrometry in the visible spectrum range is a commonly used and nondestructive method to characterize free-standing CNT films. Absorbance of free-standing CNT films at 550 nm can be experimentally correlated to the CNT film thickness without breaking the free-standing CNT film for cross-sectional thickness analysis.[11] In Fig. 4, we illustrate the linear dependence of the CNT pellicle's transmittance at 13.5 and 550 nm for different CNT types. The coefficient of this linear correlation depends on the CNT pellicle composition (CNT type, size, and purity) and film microstructure (packing density and bundling). Knowing this relation for a specific CNT type enables tuning of the CNT density during the fabrication process for a specific target EUVT.

2.3 *CNT Film Composition*

Besides the areal density of CNTs within the membrane, the composition of the CNT pellicle also plays an important role on its optical properties. A CVD approach, often used for the CNT growth, typically requires a combination of a carbon-containing reaction gas (e.g., carbon monoxide) with a metal catalyst [e.g., iron (Fe)] to form a CNT inside a high-temperature reactor furnace. If the CNTs are not purified post-growth, then the CNT film will inevitably contain metal nanoparticles. As shown in the transmission electron microscopy (TEM) image of SWCNTs in the inset of Fig. 5, most of the metal catalyst nanoparticles are embedded into the graphitic carbon shell and are <10 nm in diameter. Yet, also slightly larger inactive catalyst particles as by-product of the synthesis can be present depending on the growth conditions. Figure 5 shows the elemental composition of four different unpurified SWCNT membranes measured by the Rutherford backscattering spectrometry (RBS).[12] In the RBS characterization of free-standing CNT films, the transmitted beam was guided away in the forward direction not to contribute to the backscattering spectrum, and a multidetector assembly was used to improve the limit-of-detection and to decrease the measurement time.[13] All SWCNT samples were

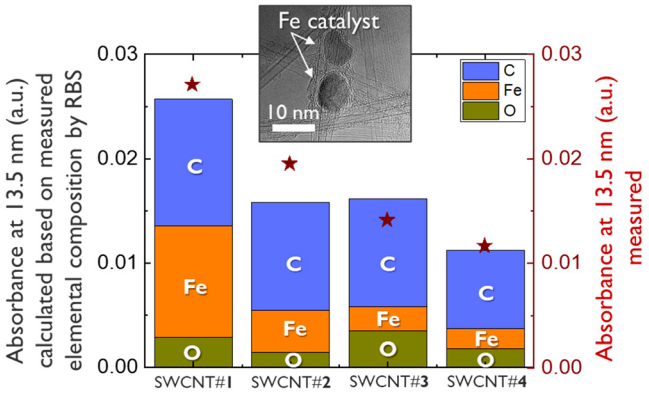

Fig. 5 Absorbance calculated based on the measured elemental composition by RBS using CXRO database (columns) and based on the measured EUVT (stars) for different types of unpurified SWCNT pellicle samples.

prepared using the floating catalyst CVD technique with different synthesis conditions and collection time (density of SWCNT#1,2 > SWCNT#3,4). Based on the compositional analysis of these samples, the corresponding thin film EUV absorbance was calculated using x-ray transmission database from the Center for X-Ray Optics (CXRO) at Lawrence Berkeley National Laboratory[14] ($A_{13.5} = -\log_{10} T_{13.5}$). This composition-based absorbance was compared with the measured absorbance for the same samples (Fig. 5). We found a good correlation between the experimental and the calculated absorbances, from which it is visible that the absorbance decreases with the decrease of the carbon content (absorbance of SWCNT#1,2 > SWCNT#3,4). In addition, the contribution of Fe (originating from the metal catalyst) to the increase in the absorbance of the pellicles is clear. Therefore, the purification of CNTs is beneficial to increase the EUVT of the CNT pellicles.

2.4 *Role of CNT Bundling*

Due to their high surface energy, individual CNTs tend to agglomerate during the fabrication process forming bundles that are held together by van der Waals forces. Such CNT bundles can be tens of nanometers in diameter and tens of micrometers in length. TEM images in Fig. 6 give an example of a SWCNT bundle [Fig. 6(a)] and average bundle size variation based on changing the pellicle fabrication parameters [Fig. 6(b)].

The bundling of CNTs is an important parameter, which can have a high impact on many membrane properties. An increase in CNT bundling in the membrane results in an improvement in the mechanical strength of the pellicle as well as its chemical durability in the etching environment. However, at the same time CNT bundling leads to an increase in the EUV light scattering in the numerical aperture (NA), which creates flare, and increased gap size, which influences the ability of the pellicle to stop particles. Some of the CNT pellicle properties can be modeled

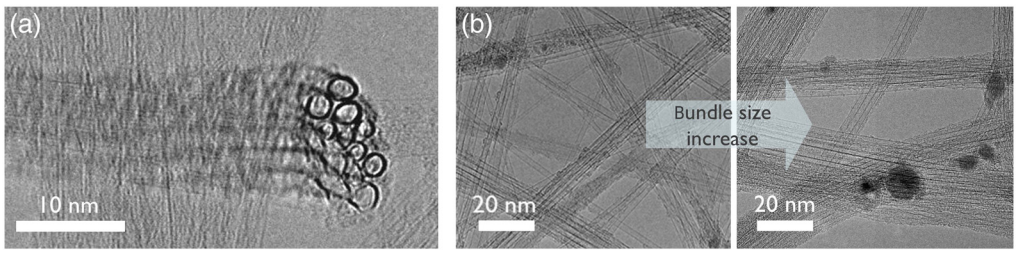

Fig. 6 TEM images demonstrating (a) SWCNT bundle in cross-section consisting of 10 to 12 individual CNTs and (b) variation of average SWCNT bundle size. Note that an SWCNT film is not purified therefore metal catalyst particles are present.

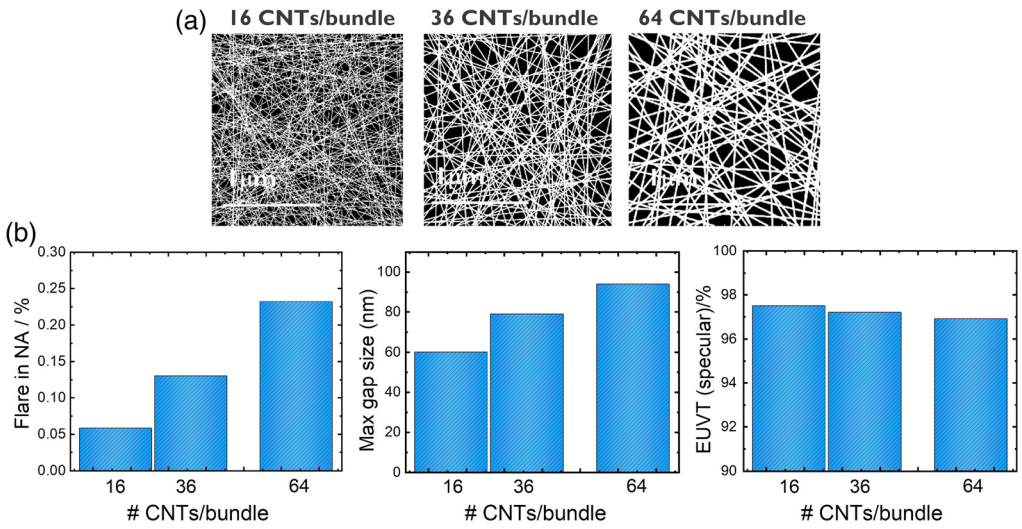

Fig. 7 (a) Simulation of CNT membrane microstructure with CNT bundling, where CNTs are shown as straight lines in random orientation. (b) Modeling-based variation of the CNT pellicle properties, i.e., flare into the NA, maximum gap size of the CNT network, and specular EUVT with respect to the amount of CNTs per bundle.

with respect to the CNT bundling degree, as was described in our earlier work.[7] Geometrical parameters such as gap size can be modeled by considering the CNTs as straight lines. With a given EUVT, the total CNT length within a specific area, e.g., $2 \times 2\ \mu m^2$, can be calculated based on the geometrical considerations of how carbon atoms are stacked in the nanotube. This total length can be distributed in random orientation over that area, providing a visual interpretation similar to SEM images [Fig. 7(a)]. In case of bundling, the effective length will be reduced by the (average) number of CNTs per bundle, which results in a different visual configuration and gap size distribution. Optical parameters such as EUVT and flare into the NA can also be modeled. In this model, the CNT is simplified by an infinitely long and straight cylinder with a given diameter and optical constant. In this representation, the absorption and scatter of an incoming electromagnetic wave can be calculated analytically per unit cylinder length.[15,16] To include the impact of bundling, the absorption and scatter of the bundle is simplified to that of one cylinder with a volume equivalent diameter. As an example, in Fig. 7, we compare the modeled properties of a CNT pellicle for constant CNT density but varying the bundle size from 16 CNTs/bundle over 36 CNTs/bundle to 64 CNTs/bundle. The results indicate that the CNT pellicle properties are influenced by the CNT bundling within the membrane and can be tuned by defining the optimum bundling degree based on the simulations. Experimentally, controlling of the bundling within a random CNT network is challenging but possible by tuning the synthesis conditions[17] and pellicle fabrication parameters.

2.5 *Thermal Properties*

When the pellicle is heated during exposure caused by the absorption of the EUV radiation, there are limited paths to dissipate that heat in the scanner conditions. Heating of thin film pellicle at high EUV powers can induce mechanical stress associated with the thermal expansion of the material[18] and facilitate chemical degradation. Radiation (emissivity) is the primary mechanism to release heat since other pathways are almost negligible; therefore, materials with higher emissivity will result in lower maximum temperatures when exposed with the same power and are expected to withstand higher thermal loads in the scanner.[19] According to Kirchoff's law, the emissivity (ε) is equal to the absorbance at any wavelength. Moreover, since the heat loss by radiation will be present at infrared (IR) wavelengths, a technique such as Fourier transform IR spectroscopy using a combination of a reflection measurement $R(\lambda)$ and transmission measurement $T(\lambda)$ can be applied to calculate the emissivity where $\varepsilon(\lambda) = 1 - R(\lambda) - T(\lambda)$.[20] A first-order approximation for the wavelength-independent emissivity (ε_o) is the average of $\varepsilon(\lambda)$ over

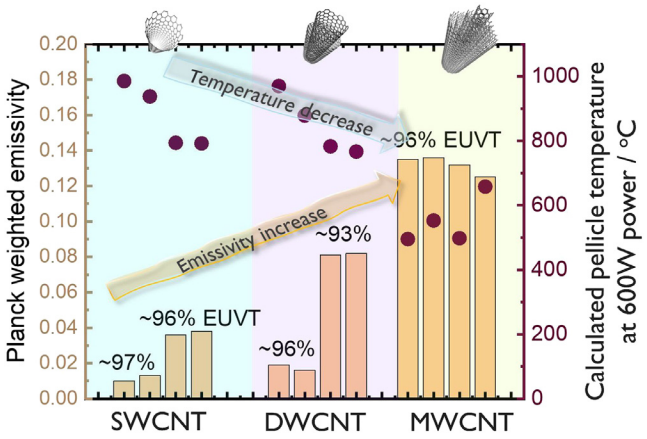

Fig. 8 Measured emissivity (columns) versus calculated pellicle temperature at 600 W source power (dots) for SWCNT, DWCNT, and MWCNT pellicles. Corresponding EUVT values are displayed within the plot.

the expected IR wavelength range, e.g., 1 to 10 μm. In thermal equilibrium, the absorbed power in the pellicle will equal the power lost, and an approximation of the pellicle temperature can be calculated. To first order, the convection can be ignored, and the radiated power, $P_{\text{radiation}}$, is given by the Stefan–Boltzmann law: $P_{\text{radiation}} = \varepsilon\sigma S(T^4{}_{\text{max}} - T^4{}_{\text{env}})$, where σ is the Stefan–Boltzmann constant, S is the exposed slit area of the pellicle, T_{max} is the maximum temperature of the pellicle in equilibrium, and T_{env} is the environment temperature.[19] To improve the model, the conduction of heat with the scanner gas environment is also included (i.e., transfer of vibrational energy from CNT to the gas molecules at low pressure). Moreover, Planck's law for radiation of a black body at a certain temperature is used to create a wavelength-weighted distribution of emitted radiation, $\varepsilon(\lambda)$. Starting with T_{o} and this Planck weighted $\varepsilon(\lambda)$, a second-order correction of pellicle emissivity and temperature is possible. This is iterated until convergence to estimate emissivity and pellicle temperature.

The relationship between the Planck-weighted emissivity and the calculated pellicle temperature is plotted for three CNT pellicle types in Fig. 8. As emissivity increases, the temperature calculated for 600 W source power decreases. The absolute value of the calculated temperature is dependent on a number of assumptions and measurement errors; however, the relative temperature trends are expected to remain valid. It is visible that MWCNT pellicles tend to have higher emissivity as compared with SWCNT pellicles, resulting in the lower expected pellicle temperature. It is worth noting that for a given pellicle type, lower EUV transmittance (i.e., higher absorbance) associated with denser CNT pellicles typically will increase emissivity. If this increase is proportionally higher than the EUV absorbance increase, this can reduce the pellicle temperature under exposure.

3 Lifetime Considerations: Uncoated CNT Pellicle

The mechanical, thermal, and chemical stability of the EUV pellicle together determine its lifetime. This section will review each in turn.

3.1 *Mechanical Stability*

An EUV pellicle must withstand the pressure changes during handling. To fulfill the EUV transparency requirement, thin film pellicle membranes (e.g., poly-Si and SiN) have a membrane thickness typically <30 nm.[18,21] With the decrease of the membrane thickness, the maximum pressure load tolerated before rupture is reduced.[1] Such thickness-dependent deflection is not that clear for a porous transparent CNT membrane. In fact, even the concept of a single thickness is challenged by the network of CNTs. The flow of gas through small gaps in the CNT mesh

minimizes the deflection of the CNT pellicle due to the reduction of the pressure difference across the membrane. This desirable characteristic improves its mechanical stability.[1] Recently performed CNT EUV pellicle exposure tests at the NXE EUV scanner at IMEC demonstrated the ability of the CNT EUV pellicles to withstand scanner handling and pump/vent cycles.[6]

3.2 *Thermal and Chemical Stability*

Modern lithography tools operate in an environment where a low-pressure hydrogen gas is introduced.[22–24] The hydrogen-containing gas is ionized by the absorption of high energy EUV photons (92 eV) and plasma is created as a by-product, which consists of energetic photoelectrons, ions, and radicals.[24,25] EUV-induced plasma in hydrogen was shown to effectively clean carbon contamination.[26] Investigating the influence of hydrogen-based plasma and high energy EUV photons on the transparent CNT membranes offline (outside of the scanner) is challenging. The main challenge is mimicking the scanner environment for the pellicle lifetime studies. One approach is to isolate nonplasma-related processes, i.e., pellicle heating caused by the absorption of the EUV radiation, and the chemical stability of CNTs in hydrogen plasma environment.

In vacuum, a 97% EUV transparent CNT membrane was shown to withstand high thermal loads up to >1000 W EUV power equivalent exposures (>20 W/cm^2).[27]

To investigate the chemical stability, the CNT material on a silicon substrate was exposed to hydrogen radicals (H*) at room temperature. H* were generated by the catalytic decomposition of H_2 gas (15 Pa) using a tungsten hot-wire catalyzer. The exposure time was varied and Raman spectroscopic measurements of the sample after several exposure steps were performed (Fig. 9). Raman spectroscopy is an effective technique to probe structural modifications of the CNT sidewalls and crystalline quality, allowing to detect small changes in the CNT crystal structure.[28] Raman spectra were collected using a Horiba Jobin-Yvon LabRAM HR800 Raman spectrometer with 2.33-eV laser excitation energy through a 10× objective. Raman spectra of CNTs typically consist of the G-band, related to the vibration of sp^2-bonded carbon atoms in a two-dimensional hexagonal lattice, and the D-band, related to defects on the nanotube walls and non-CNT impurities.[29] The intensity ratio of the two bands (I_D/I_G) is a sensitive measure of the CNT structural quality (or defect density) and the relative amount of amorphous carbon.

Here, we focus on the analysis of SWCNTs but note that a similar effect was observed for MWCNTs. The as-grown SWCNT material possesses good initial structural quality ($I_D/I_G \sim 0.02$). When exposing CNTs to H* at room temperature, the *G* peak intensity decreases and the *D* peak intensity increases. The most pronounced change occurs after the first hour of exposure, where the I_D/I_G ratio increase reflects the introduction of defects and the onset of CNT etching (Fig. 9). Measurements after the 56 h of H* exposure indicate that at some point CNT material removal starts to dominate over the formation of defects; therefore, the intensity of

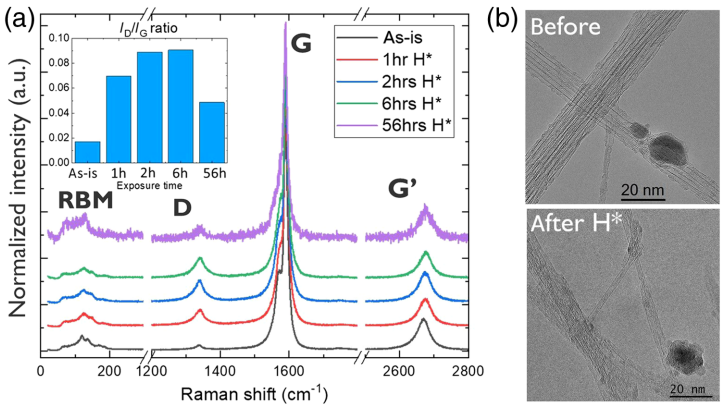

Fig. 9 (a) Raman spectra before and after exposing SWCNTs to hydrogen radicals (H*) at room temperature. Inset: I_D/I_G ratio variation as a function of the exposure time. (b) TEM images of SWCNTs before and after 56 h exposure to H* at room temperature.

the Raman signal overall decreases. Most of the CNT material was removed after 110 h of exposure to H*. The damage and etching of the CNTs can be recognized in the TEM images of the exposed sample [Fig. 9(b)] and is in agreement with the literature.[30]

The relevance of these results for understanding the CNT pellicle lifetime in the scanner environment depends on the chosen experimental conditions. In the scanner, the CNT pellicle is exposed to an EUV-induced hydrogen-based plasma and at the same time is heated due to the absorption of EUV radiation. To probe the synergistic effect of EUV radiation and plasma on the CNT membrane, uncoated CNT pellicles were dynamically exposed to EUV light at 600-W EUV scanner source power equivalent in the scanner representative gas environment. These exposures were performed at the beamline operated by the Physikalisch-Technische Bundesanstalt (PTB) at the BESSY II synchrotron facility.[31] To emulate the EUV source powers, apertures were used to select a specific part of the beamline's spot and the distance from the focus was adjusted.[31]

3.3 *EUV Scanner-Like Environment at 600 W Equivalent Source Power*

Nonscanner (offline) exposures of CNT pellicles enable the study of CNT material changes under concurrent exposure to EUV radiation and EUV-induced plasma in the scanner-like gas environment, although it is important to note that the exposure conditions remain an approximation of the scanner conditions and gases.

3.3.1 *SWCNT pellicle case: short exposure*

In this experiment, we exposed an uncoated SWCNT pellicle to 600-W EUV scanner source power equivalent (EUV power density ~12 W/cm^2) in a hydrogen-based gas environment and varied the exposure time. For these exposures, test pellicle samples with the free-standing CNT membrane of 10×10 mm^2 were used. To ensure that the pellicle remains mechanically strong for post-exposure analysis, we started with exposing the sample to EUV beam for 15 min. Changes in EUVT before and after the exposure were monitored (Fig. 10). The EUV beam was scanned across the middle part of the sample, the so-called IN-beam region. Since plasma, formed by the ionization of the background gas, is expected to be larger in dimensions than the EUV beam itself,[24] the OUT-beam region of the sample, exposed to plasma only, was also analyzed. The CNT material changes of IN-beam and OUT-beam regions were compared. Figure 10 shows EUVT mapping for SWCNTs with two different CNT densities, i.e., SWCNT with ~97% EUVT and SWCNT with 95.5% EUVT, before and after their exposure. A small EUVT increase is observed for the IN-beam region for both sample types with a slightly

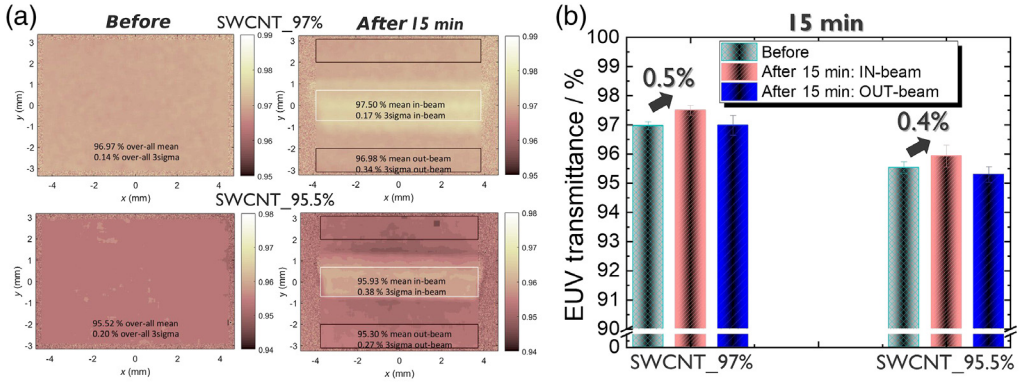

Fig. 10 (a) EUV transmittance maps (21×21 pixel average) for SWCNT pellicles with two different densities (SWCNT pellicle with EUVT 97% and SWCNT pellicle with EUVT 95.5%) before and after exposure to the EUV scanner-like environment at 600-W equivalent source power for 15 min. EUV beam was scanned across the middle region of the sample (IN-beam). (b) Corresponding EUV transmittance before and after the exposure (error bar is 3σ value based on the EUVT maps). IN-beam and OUT-beam regions after exposure are analyzed separately.

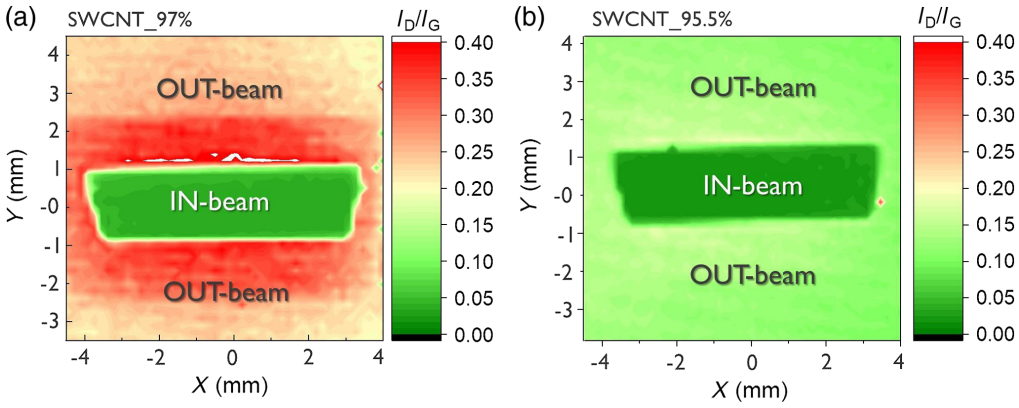

Fig. 11 Raman mapping of I_D/I_G ratio for SWCNT pellicle samples with (a) 97% EUVT and (b) 95.5% EUVT, after their exposure to the EUV scanner-like environment at 600-W equivalent source power for 15 min. EUVT maps of the corresponding samples are shown in Fig. 10.

higher increase for the lower density sample (SWCNT_97%) than the higher density one (SWCNT_95.5%). No change (for SWCNT_97%) or a slight decrease (for SWCNT_95.5%) in EUVT is observed in the OUT-beam region.

Furthermore, various material analysis techniques were applied to study the CNT material changes with exposure. Interestingly, Raman spectroscopic measurements of the free-standing CNT membranes after 15 min exposure reveal a noticeable effect on the CNT material. For these measurements, the entire CNT membrane was raster-scanned, creating a full-map Raman spectrum with data collected at every 200 μm step. The maps of the I_D/I_G ratio in Fig. 11 for two SWCNT pellicles with different EUVT show a clear signature of the CNT pellicle exposure pattern, which correlates strongly with the corresponding EUVT mapping results of Fig. 10. An increase in the I_D/I_G ratio (or defect density) is observed in the OUT-beam region for both samples.

Further Raman spectroscopy at different excitation energies was performed, and the results were compared with the reference (unexposed) sample (Fig. 12). In addition to the I_D/I_G ratio, the ratio of the G′-band to D-band intensities ($I_{G'}/I_D$) was used as an indication of sample purity,

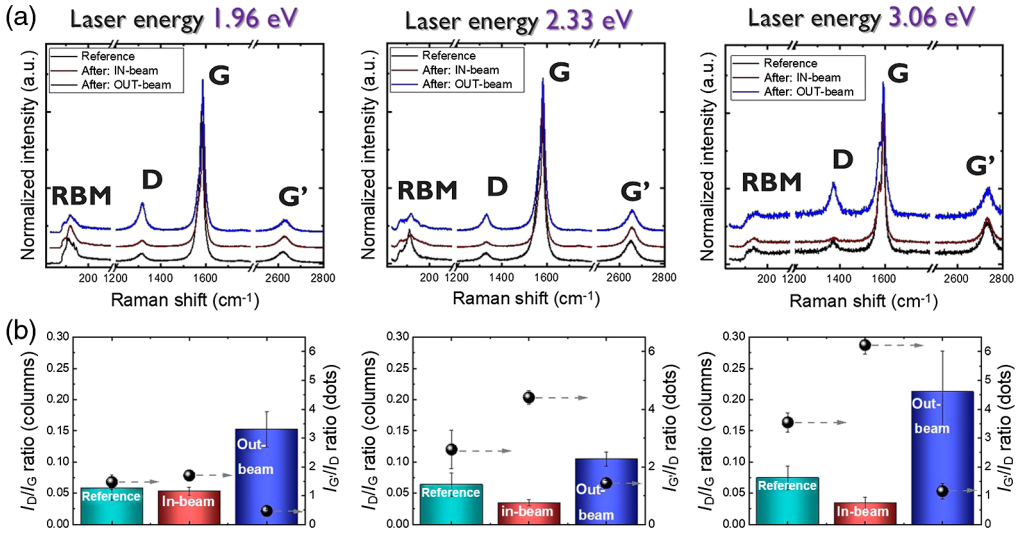

Fig. 12 (a) Examples of Raman spectra for SWCNT pellicle with EUVT 97% measured with different laser energies (i.e., 1.96, 2.33, and 3.06 eV) after exposure to the EUV scanner-like environment at 600-W equivalent source power for 15 min, compared with a reference CNT sample of the same density. (b) Corresponding I_D/I_G and $I_{G'}/I_D$ ratio analysis. An error bar for the reference sample takes into account possible variations between similar samples.

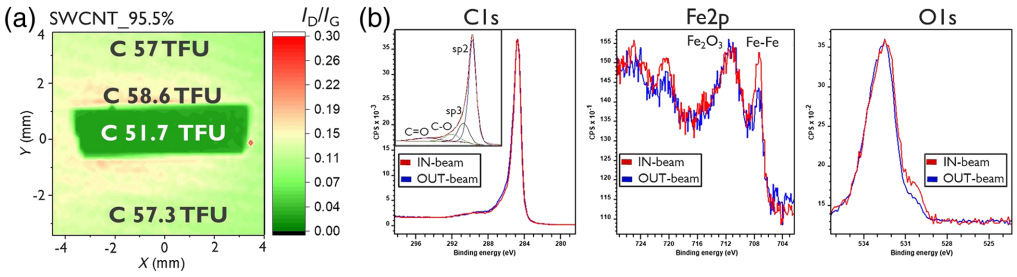

Fig. 13 (a) Raman mapping of I_D/I_G ratio and corresponding initial carbon (C) amount in thin film units (TFU) measured by EBS for a SWCNT pellicle with EUVT 95.5% exposed to the EUV scanner-like environment at 600-W equivalent source power for 15 min. The statistical error on C measurements was 1.1%. (b) Representative XPS spectra of IN-beam and OUT-beam regions of the exposed SWCNT pellicle sample with EUVT 95.5% for the different energy regions, i.e., C1s, Fe2p, and O1s. The XPS spectra were normalized to achieve an easier comparison. Relative amounts can be retrieved from Table 1.

increase of which points to the reduction of contaminants.[32] G′-band spectra arise from a two-phonon, second-order Raman scattering process and is not sensitive to tube defects.[28,32] A decrease in I_D/I_G ratio, complemented by the increase in $I_{G'}/I_D$, in the IN-beam sample region, where CNT pellicle is expected to heat up with the absorption of the EUV radiation, as compared with the reference suggest sample purification, cleaning and possibly defect healing or defect etching. SWCNT purification via removal of amorphous carbon and defect healing using laser exposures at different wavelength and environments was described in the literature.[32–34] In these experiments, the use of an optimum irradiance power density before the onset of the CNT damage and the presence of an oxidizing environment were critical.[32,34,35] In the OUT-beam region of the sample, an increase in the I_D/I_G ratio and concurrent decrease in $I_{G'}/I_D$ reveal CNT damage and contamination. To have a better view of the CNT membrane changes, Raman analysis was supplemented with the chemical composition analysis of the exposed pellicles using elastic backscattering spectroscopy (EBS), x-ray photoelectron spectroscopy (XPS), and time of flight secondary ion mass spectrometry (ToF-SIMS).

EBS measurements, using proton beam as probe projectiles at 2 MeV, were applied to quantify the elemental composition of the SWCNT pellicle (SWCNT_95.5%) in the two regions. This approach enables accurate quantification of such light elements as carbon,[36] dominant element in CNT films. Figure 13(a) shows EBS results for carbon (C) in thin film units (TFU or 1E15 at/cm^2) displayed on top of the Raman I_D/I_G map of the corresponding sample. Each value represents an average of three to four EBS measurements performed in the corresponding regions. A higher carbon amount OUT-beam as compared to the IN-beam was measured.

XPS measurements were performed to investigate the surface chemistry of the SWCNT pellicle IN-beam versus OUT-beam after exposure at three to five locations within the corresponding regions, and representative spectra are shown in Fig. 13(b). XPS measurements were carried out in angle-integrated mode using a Theta300 system from Thermo Instruments. A monochromatized Al Kα x-ray source (1486.6 eV) and a spot size of 100 μm were used. The XPS survey spectra reveal the presence of C, O, and Fe, in line with the EBS analysis. A small amount of surface contaminants such as F, N, and Si was also detected by XPS. Analysis of the C1s peak of the XPS spectrum distinguishes sp^2-hybridized graphite-like carbon of the CNT walls, sp^3-hybridized diamond-like carbon associated with defect sites, and carbon atoms with C=O and C-O groups (Table 1). To achieve a repeatable fitting procedure, the main C1s peak was set at 284.8 eV and fixed binding energy differences relative to the main peak were set for the other components of the spectra (0.9 eV for sp^3, 2.1 eV for C-O, and 4.7 eV for C=O). It should be noted that the identification of the peak at ~285.7 eV as sp^3 is not unique and some oxygen-bounded carbon could also contribute to the intensities at that energy. The intensity of the components attributed to C-O groups on the C1s spectra was higher in the OUT-beam versus IN-beam regions. This was also accompanied by an increase of the measured atomic percentage of O in the OUT-beam region (Table 1). In addition, a lower intensity of unoxidized Fe contribution on the Fe2p spectra (Fe–Fe at ~707 eV) OUT-beam compared to IN-beam was

Table 1 Relative atomic concentrations (at. %) as calculated using the fits on the C1s, O1s, Fe2p, N1s, F1s, and Si2p XPS curves for SWCNT pellicle exposed to the EUV scanner-like environment at 600-W equivalent source power for 15 min.

	C sp2	C sp3	C–O	C=O	O	Fe	N	F	Si
IN-beam	65.1	15.3	5.9	7.3	4.0	1.6	0.2	0.0	0.7
OUT-beam	61.0	15.4	7.9	6.3	6.6	1.4	0.2	0.1	1.1

observed. This change in the chemical state of Fe could be explained by damage of the carbon coating surrounding the catalyst nanoparticles OUT-beam, likely to be etched sooner than the nanotube wall under the exposure to hydrogen-based plasma.[37] Once exposed to air, the nanoparticles OUT-beam are further oxidized. The higher intensity of metallic Fe in the IN-beam region could be the result of iron oxide reduction and carbon shell repair around the particles. No clear change in the amount of Fe IN-beam versus OUT-beam could be measured by EBS, nor observed in SEM.

Moreover, a ToF-SIMS analysis was performed with a ToF-SIMS V system (ION-TOF GmbH, Münster, Germany) using a 30-kV Bi_1^+ beam as a primary ion source. Another SWCNT pellicle sample exposed under the same conditions was analyzed. ToF-SIMS results indicate a lower intensity of C, O, and surface contaminants in the IN-beam compared to OUT-beam regions of SWCNT samples (Fig. 14). SEM observations did not reveal significant changes IN-beam versus OUT-beam, although for certain SWCNT pellicle types several broken CNT bundles OUT-beam were observed. CNT etching IN-beam does not seem to occur for short exposure times.

In summary, transmission, spectroscopic, and chemical mapping of the SWCNT pellicle exposed for 15 min to 600-W equivalent EUV scanner source power in the scanner-like gas environment demonstrate an initial CNT purification, likely removal of non-nanotube impurities IN-beam causing a minor EUVT increase. Hydrogen etching is expected to start on carbon-based contamination, which can include amorphous carbon, fullerene-like particles, carbon atoms on the defective SWCNTs, and pentagonal carbon at the end of the CNTs or around catalyst particles.[37] Under EUV radiation in the presence of H_2 gas in EUV lithography, carbon contamination is known to be removed via physical and chemical sputtering by ionized species.[22] The onset of CNT damage is clearly observed OUT-beam together with an increase of carbon and oxygen content as compared to the IN-beam. Two concurrent effects might occur OUT-beam, i.e., CNT damage (possibly etching) and contamination, suggesting a possible cause of no EUVT change OUT-beam or even a slight EUVT decrease for some of the exposed samples. This contamination OUT-beam could be a result of *in situ* redeposition due to the formation of volatile hydrides and redeposit of the reaction products on other surfaces,[24] or *ex situ* with

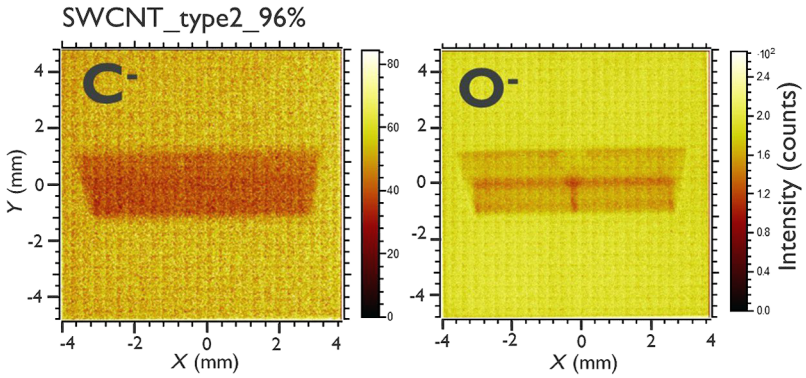

Fig. 14 Carbon (C) and oxygen (O) ion mapping obtained by ToF-SIMS for SWCNT pellicle with 96% EUVT after exposure to the EUV scanner-like environment at 600-W equivalent source power for 15 min.

the exposure to air where oxygen and other species could be adsorbed at the newly generated defect sites. It is important to note that EUVT and other measurements of the SWCNT pellicles after EUV radiation were performed after the sample was exposed to air, therefore *in-situ* measurements would be important to better understand the effect of EUV + H_2-based gas environment on the CNT pellicles.

Overall short 15 min exposure of the uncoated SWCNT pellicle to the representative pellicle environmental conditions at 600-W source power equivalent yielded only minor structural changes to the CNT pellicle membrane. The CNT pellicles remained mechanically strong and were able to withstand multiple cases of pressure changes when loading the samples to various material analysis tools as well as pellicle shipments.

3.3.2 *SWCNT pellicle case: longer exposure*

Keeping the EUV exposure conditions the same, i.e., 600-W EUV scanner source power equivalent in the scanner-like gas atmosphere, we increased the time that the EUV beam is scanning across the middle area of the uncoated SWCNT pellicle sample. In a similar manner as shown above, the EUVT of the pellicle was mapped before and after the exposure, where in the latter case two regions were analyzed, IN-beam and OUT-beam. Note that with this exposure, the beam size was a few millimeters wider as compared with the shorter exposures discussed in Sec. 3.3.1. The mapping results are shown in Fig. 15.

Even though the starting EUVT of this SWCNT pellicle sample was slightly lower, i.e., 93.5%, a similar trend of EUVT increase IN-beam and no significant change of EUVT OUT-beam was observed after 30 min exposure. It is clear that with the increased exposure time, a larger EUVT drift IN-beam was observed, i.e., 1.4%point EUVT increase (Fig. 15). Further, Raman and XPS mapping of the exposed sample were performed. Figure 16(a) shows the I_D/I_G ratio map of the sample where a similar trend of higher I_D/I_G ratio (or defect density) was observed in the OUT-beam region as compared to the IN-beam region. At the same time, the IN-beam region showed an increase in I_D/I_G ratio and a decrease of the $I_{G'}/I_D$ ratio (or purity index) as compared to the reference sample. The results of the Raman quality and purity indicators together with an overall decrease in the Raman signal intensity suggest that the uncoated SWCNT pellicle experienced significant damage and CNT removal under the influence of EUV

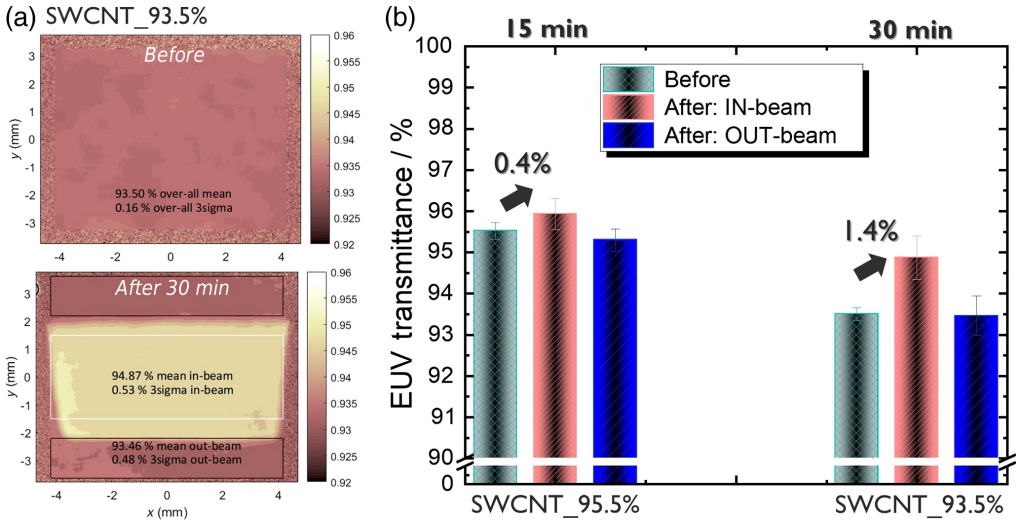

Fig. 15 (a) EUV transmittance maps (21 × 21 pixel average) for SWCNT pellicle with 93.5% EUVT before and after exposure to the EUV scanner-like environment at 600-W equivalent source power for 30 min. EUV beam was scanned across the middle region of the sample (IN-beam). (b) Corresponding EUV transmittance before and after the 30 min exposure, compared with a similar SWCNT pellicle exposed for 15 min under the same conditions (error bar is 3σ value based on the EUVT maps). IN-beam and OUT-beam regions after the exposure are analyzed separately.

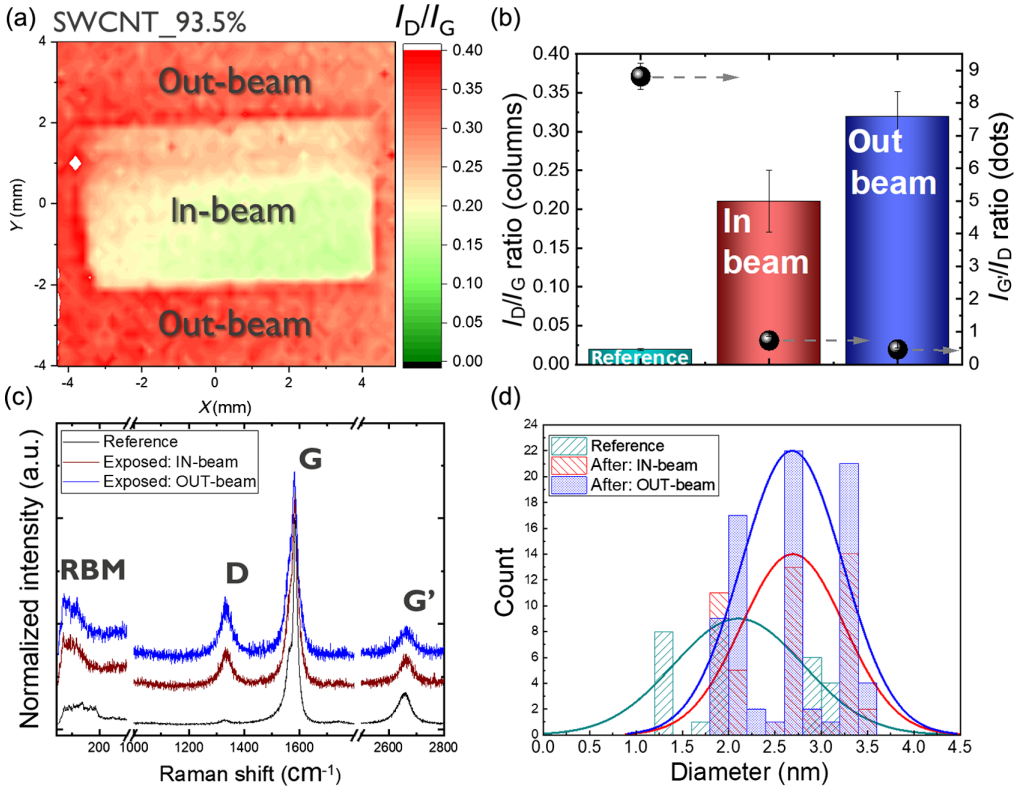

Fig. 16 (a) Raman mapping of the I_D/I_G ratio for an SWCNT pellicle with 93.5% EUVT after exposure to the EUV scanner-like environment at 600-W equivalent source power for 30 min. EUVT map of the corresponding sample is shown in Fig. 15. (b) Analysis results of Raman quality (I_D/I_G) and purity ($I_{G'}/I_D$) indicators for a reference and exposed samples IN-beam and OUT-beam. (c) Example Raman spectrum for a reference and exposed sample IN-beam and OUT-beam. (d) Distribution of SWCNT diameter for a reference and exposed samples IN-beam and OUT-beam based on the RBM mode analysis of the Raman spectrum. 2.33 eV laser energy was used for all the measurements.

+ scanner gases after 30 min exposure. The radial breathing mode (RBM) of the Raman spectra, which corresponds to the coherent vibrations of carbon atoms in the radial direction, enables an estimate of the CNT diameter, d_t ($\omega_{\mathrm{RBM}} = 234/d_t$).[28,32] A slight shift toward larger average diameter SWCNTs after the exposure was seen as compared with the reference sample [Fig. 16(d)]. These findings indicate that larger diameter CNTs are more stable when exposed to plasma, which is in line with literature observations.[30,38] Higher hydrogenation reactivity of smaller diameter CNTs is explained by their higher curvature and strain in the structure.[30]

Figure 17 shows the comparison of the C1s, O1s, and Fe2p representative XPS spectra for IN-beam and OUT-beam regions of the sample corresponding to the Raman mapping shown in Fig. 16(a). Similar observations as for the shorter exposure time were made: a larger relative C-O component on the C1s spectra and more oxygen detected OUT-beam (Table 2). It is interesting that almost no metallic Fe remained present in the OUT-beam region of the SWCNT sample with prolonged plasma exposure indicating that all carbon coatings enclosing metallic particles were damaged or removed resulting in air oxidation of the catalyst particles. It is possible that in the IN-beam region some of the Fe particles were removed after etching of the surrounding carbon shell, which could also explain the higher intensity of metallic Fe as measured by XPS and contribute to an EUVT increase IN-beam. However, due to the pellicle breakage, EBS or SEM measurements could not be performed to check this hypothesis.

This SWCNT material was further examined in TEM. Figure 18 shows a comparison of the unexposed reference sample with the exposed SWCNT material likely originating from the OUT-beam region of the sample. After prolonged exposure, uncoated SWCNTs show deformation and amorphization, contamination, local collapse of the CNTs with the disappearance of

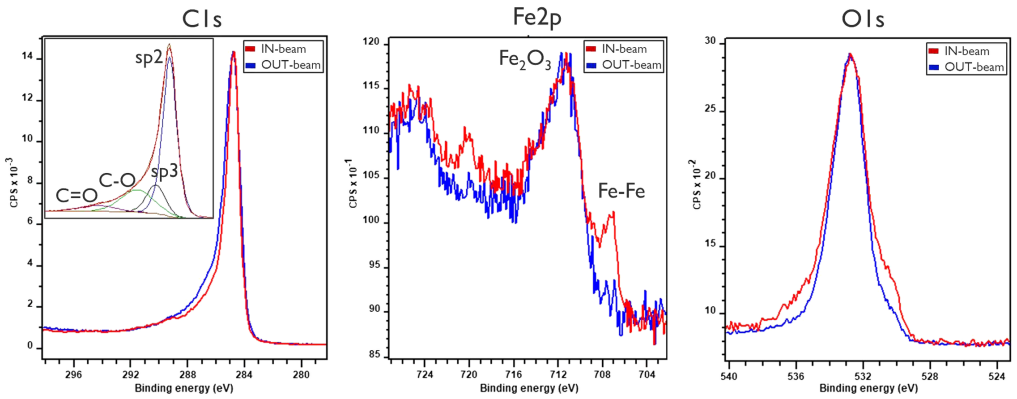

Fig. 17 Comparison of the C1s, Fe2p, and O1s representative XPS spectra IN-beam and OUT-beam for the SWCNT pellicle with 93.5% EUVT exposed to the EUV scanner-like environment at 600 W equivalent source power for 30 min. Spectra were normalized to allow a better chemical comparison. Relative amounts can be retrieved from Table 2.

Table 2 Relative atomic concentrations (at. %) as calculated using the fits on the C1s, O1s, Fe2p, N1s, F1s, and Si2p XPS curves for SWCNT pellicle exposed to the EUV scanner-like environment at 600-W equivalent source power for 30 min.

	C sp2	C sp3	C-O	C=O	O	Fe	N	F	Si
IN-beam	55.5	12.3	13.0	6.8	8.6	1.9	0.4	0.3	1.2
OUT-beam	51.7	11.8	16.1	4.5	12.6	1.4	0.4	0.4	1.2

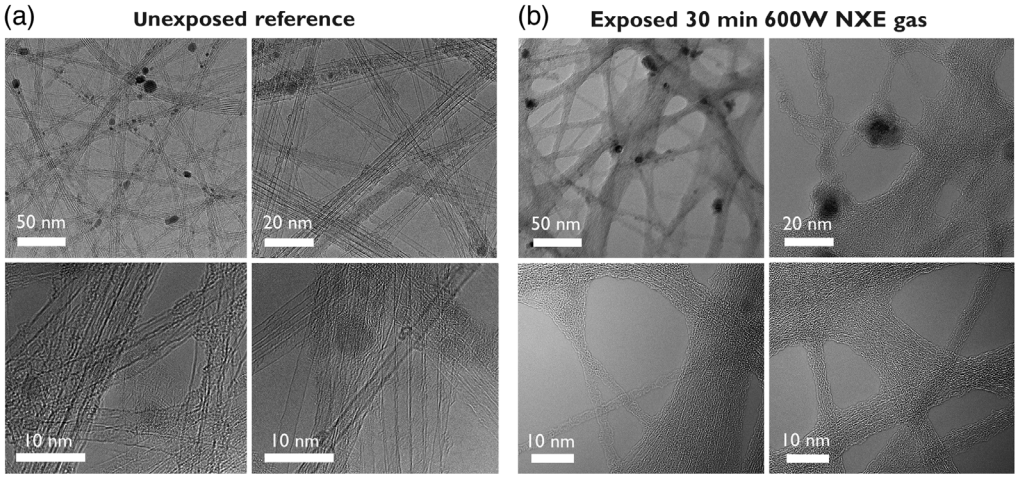

Fig. 18 TEM images comparing (a) unexposed reference SWCNT sample with (b) the one exposed to the EUV scanner-like environment at 600-W equivalent source power for 30 min.

the central hollow, fragmentation and removal of the CNTs. Individual CNTs and smaller bundles are damaged and etched first.

In summary, 30-min exposure of the uncoated SWCNT pellicle sample to the EUV scanner representative pellicle environmental conditions at 600-W equivalent source power yielded major structural changes to the CNT pellicle membrane with lower damage IN-beam as compared to the OUT-beam region. The CNT pellicles survived the exposure, sample shipment, and a number of measurements; however, due to the material modifications with exposure the pellicle became more fragile and broke with handling.

3.3.3 *MWCNT pellicle case: longer exposure*

MWCNT pellicles were also exposed in a similar manner as SWCNT pellicles to the EUV scanner-like environment at 600-W equivalent source power for 30 min. EUVT before and after the exposure was mapped [Fig. 19(a)]. The observed trend of EUVT increase IN-beam and slight EUVT decrease OUT-beam for MWCNT is similar to the trend reported above for SWCNT pellicle samples. However, it is interesting to note that for the same exposure time under the same exposure conditions a smaller EUVT drift IN-beam for MWCNT pellicles was observed, i.e., 0.7%point EUVT increase for a MWCNT pellicle versus 1.4%point increase for a SWCNT pellicle [Fig. 19(b)].

Raman spectroscopy was performed to study the MWCNT pellicle material modifications after exposure. The starting I_D/I_G ratio of MWCNTs was higher compared to SWCNTs, i.e., 0.7 for MWCNTs versus 0.02 to 0.05 for SWCNTs, suggesting more disorder in the MWCNT structure. The MWCNT quality is significantly decreased (I_D/I_G increases) after 30 min exposure in both IN-beam and OUT-beam regions [Fig. 20(a)]. XPS measurements also show a noticeable increase in the O level and C-O bonds in the OUT-beam region compared to the IN-beam region [see Fig. 20(b) and Table 3]. The MWCNT sample was purified to remove catalyst particles and consequently did not contain a measurable amount of Fe.

TEM analysis of the as-exposed MWCNT pellicle sample as compared to the unexposed reference shows significant damage to the MWCNT structure including wall deformations and formation of small ripples. However, the MWCNT cylindrical structure is preserved and few removed or broken MWCNTs are observed (see Fig. 21). This indicates that MWCNTs possess a comparatively higher structural stability and radiation tolerance than SWCNTs. Similar effects were reported in the literature for electron beam-induced surface modifications of SWCNT and MWCNTs, where a higher stability of MWCNTs toward irradiation was associated with the presence of the inner tubes that prevent the outer tubes from collapsing.[39–41]

In summary, despite a significant structural damage of the uncoated MWCNT pellicle sample revealed by Raman and TEM after 30 min exposure at 600-W equivalent source power in the EUV scanner-like gas environment, a lower EUVT drift was measured as compared to a

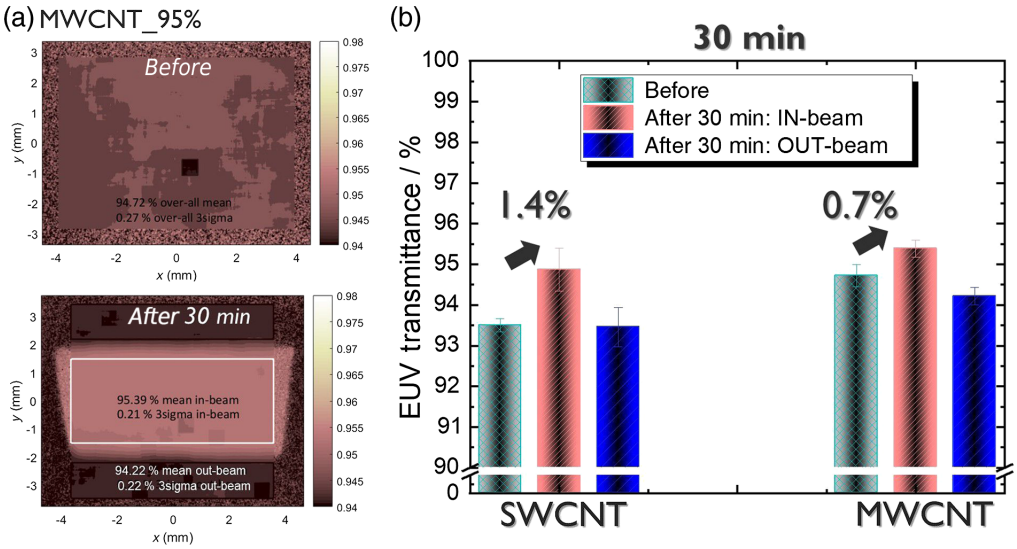

Fig. 19 (a) EUV transmittance maps (21 × 21 pixel average) for MWCNT pellicle before and after exposure to the EUV scanner-like environment at 600-W equivalent source power for 30 min. EUV beam was scanned across the middle region of the sample (IN-beam). Note that the local transmittance minima on the sample measured before the exposure is believed to be the consequence of a fall-on particle due to sample handling. (b) Corresponding EUV transmittance before and after 30 min exposure for a MWCNT pellicle, compared to a SWCNT pellicle exposed to the same conditions and time (error bar is 3σ value based on the EUVT maps). IN-beam and OUT-beam regions after exposure are analyzed separately.

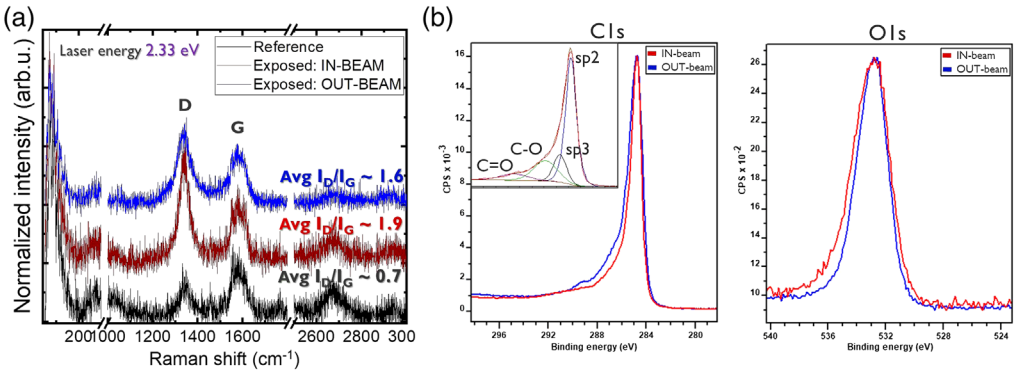

Fig. 20 (a) Example Raman spectra for a reference MWCNT pellicle and the one exposed to the EUV scanner-like environment at 600-W equivalent source power for 30 min, IN-beam and OUT-beam. 2.33 eV laser energy was used for the measurements. (b) Comparison of the C1s and O1s representative XPS spectra IN-beam and OUT-beam. Spectra were normalized to allow a better chemical comparison.

Table 3 Relative atomic concentrations (at. %) as calculated using the fits on the C1s, O1s, Fe2p, N1s, F1s, and Si2p XPS curves for MWCNT pellicle exposed at 600-W EUV power equivalent for 30 min in the scanner-like environment.

	C sp2	C sp3	C-O	C=O	O	Fe	N	F	Si
IN-beam	56.6	14.7	12.1	8.3	7.1	0.1	0.4	0.2	0.5
OUT-beam	51.4	12.5	16.9	6.0	11.8	0.0	0.7	0.2	0.5

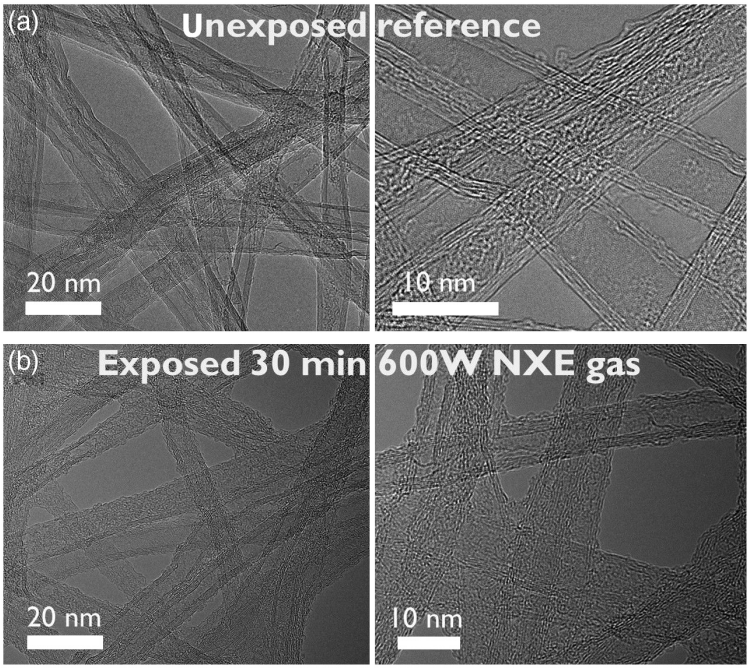

Fig. 21 TEM images comparing (a) unexposed reference MWCNT sample with (b) the one exposed to the EUV scanner-like environment at 600-W equivalent source power for 30 min.

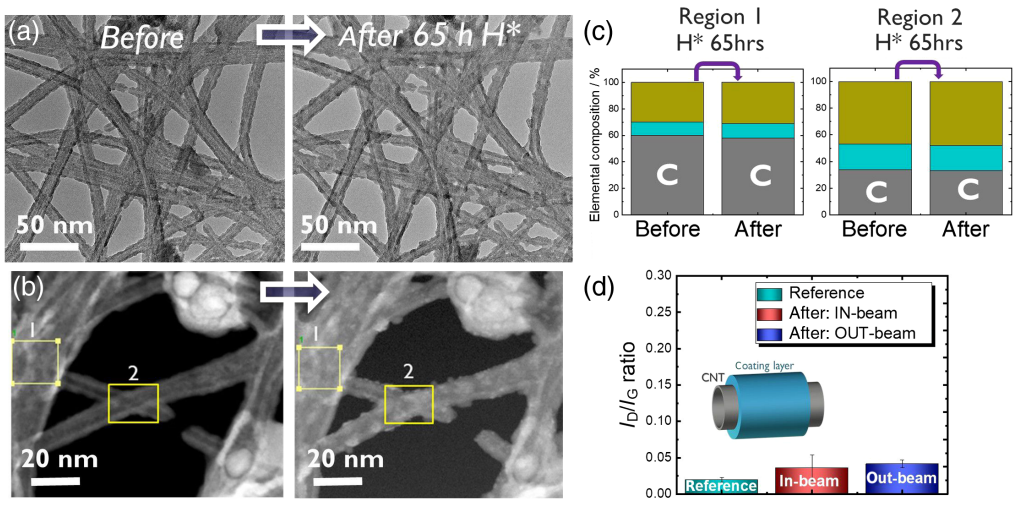

Fig. 22 (a) TEM and (b) scanning TEM images of coated SWCNTs and bundles before (left) and after (right) exposure to H* (15 Pa) for 65 h at room temperature. (c) Chemical composition locally measured by EDS before and after H* exposure for two regions as marked in (b). (d) Raman I_D/I_G ratio analysis of the coated SWCNT pellicle (91% EUVT) before and after exposure to the scanner-like gas environment at 300 W for 30 min IN-beam and OUT-beam.

SWCNT pellicle under the same exposure conditions explained by less CNT material removal as observed in TEM.

4 Coating CNT Pellicle

Coating the CNT pellicle is a potential path to reduce the CNT structural damage by hydrogen-containing plasma and to extend the pellicle lifetime in the EUV scanner environment. Our preliminary results showed the ability of the coating to preserve the CNT structure when exposing a coated SWCNT material (~90% EUVT) to H* (15 Pa) at room temperature for 65 h. As revealed by TEM observations of the same area (before and after the exposure), coated CNT material remained intact after a 65 h exposure to H* [Figs. 22(a) and 22(b)], whereas an uncoated SWCNT reference was significantly damaged and largely removed already after 56 h of the same exposure as discussed in Sec. 3.2. Chemical composition of the two regions of coated CNTs before and after exposure was evaluated by energy-dispersive x-ray spectroscopy (EDS). EDS done at the thicker bundle (region 1) showed higher carbon (C) percentage than at the thinner one (region 2), but in both regions no measurable change in the chemical composition of the coated CNTs due to H* exposure was observed [Fig. 22(c)]. Coated CNT pellicles were also exposed at PTB to the scanner-like gas environment at 300 W EUV source power equivalent (EUV power density ~6 W/cm^2) for 30 min. Figure 22(d) shows I_D/I_G ratio analysis from Raman mapping for the coated SWCNT pellicle with 91% EUVT before and after its exposure. Coating preserved the structural quality of SWCNT pellicles relative to the uncoated case. This demonstration is important, and further exploration and optimization of possible coating options to fulfil the EUV pellicle requirements for the scanner environment are the subject of our ongoing research.

5 Conclusions

CNTs are promising building blocks for a highly configurable EUV pellicle. Different CNT types were tested for the pellicle application, i.e., SWCNTs, DWCNTs, and MWCNTs. All CNT types allow to achieve high EUV transmission with acceptable uniformity. CNT material type, density, bundle size, and composition (purity) are parameters examined to tailor the CNT EUV pellicle properties for optimal performance.

Uncoated CNT pellicles survive 600-W equivalent source power (~12-W/cm^2 EUV power density) exposure in the EUV scanner-like gas environment. However, material analysis after exposure reveals CNT structural modifications leading to the degradation of the mechanical strength of the pellicle with prolonged exposures. The degree of these changes under the same exposure conditions is modulated by various CNT material parameters including initial structural quality, density, diameter, bundling, purity, and surface contamination. MWCNT pellicles have lower EUVT drift compared with SWCNT pellicles and maintain their cylindrical structure better than SWCNTs under the same exposure conditions. However, improvements are still needed in terms of the mechanical strength and structural quality of current MWCNT pellicles.

The CNT pellicle performance in a scanner depends not only on the CNT type and material parameters but also largely on the exposure conditions and gas environment. The influence of EUV radiation and hydrogen-based gas environment on the uncoated CNT pellicle observed in this study is a combination of chemical effects governed by the reactive species produced in the plasma, and photothermal processes involving the CNT pellicle heating with the absorption of the EUV radiation. More in-depth investigation of the mechanisms involved in CNT material modification is necessary.

In addition to CNT membrane optimization, coating of the CNT pellicle is a potential route toward CNT pellicle lifetime extension in the scanner environment. The protection of CNT material from structural degradation by means of coating was shown. Further optimization of both the CNT pellicle material and the coatings is in progress to fulfill the EUV pellicle requirements for high-volume manufacturing with EUV lithography.

Acknowledgments

We would like to thank CNT suppliers: Lintec NSTC, Canatu Oy, and Institute of Metal Research (IMR). We appreciate the cooperation and assistance of the ASML pellicle research team. The authors acknowledge Frank Scholze and Christian Laubis from PTB for useful discussions and Wim Arnold Bik from Detect99 for EBS measurements.

References

1. M. Y. Timmermans et al., "Free-standing carbon nanotube films for extreme ultraviolet pellicle application," *J. Micro/Nanolithogr. MEMS MOEMS* **17**(4), 043504 (2018).
2. E. E. Gallagher et al., "CNTs in the context of EUV pellicle history," *Proc. SPIE* **10583**, 105831E (2018).
3. H. J. Levinson and T. A. Brunner, "Current challenges and opportunities for EUV lithography," *Proc. SPIE* **10809**, 1080903 (2018).
4. I. Pollentier et al., "EUV scattering from CNT pellicles: measurement and control," *J. Micro/Nanopatterning, Mater. Metrol.* **20**(2), 021007 (2021).
5. M. Keshet et al., "Enabling non-actinic EUV mask inspection using carbon nanotube pellicle," *Proc. SPIE* **11609**, 1160910 (2021).
6. J. Bekaert et al., "CNT pellicle: imaging results of the first full-field EUV exposures," *J. Micro/Nanopatterning, Mater. Metrol.* **20**(2), 021005 (2021).
7. I. Pollentier et al., "The EUV CNT pellicle: balancing material properties to optimize performance," *Proc. SPIE* **11323**, 113231G (2020).
8. M. Y. Timmermans et al., "CNT EUV pellicle tunability and performance in a scanner-like environment," *Proc. SPIE* **11609**, 116090Y (2021).
9. A. G. Nasibulin et al., "Multifunctional free-standing single-walled carbon nanotube films," *ACS Nano* **5**(4), 3214–3221 (2011).
10. M. D. Lima et al., "Ultra-low density, nanostructured free-standing films for EUV pellicles," *Proc. SPIE* **11517**, 1151709 (2020).
11. G. A. Ermolaev et al., "Express determination of thickness and dielectric function of single-walled carbon nanotube films," *Appl. Phys. Lett.* **116**, 231103 (2020).
12. J. Meersschaut and W. Vandervorst, "High-throughput ion beam analysis at IMEC," *Nucl. Instrum. Methods Phys. Res. Sect. B* **406**(Part A), 25–29 (2017).

13. G. Laricchiuta et al., "High sensitivity Rutherford backscattering spectrometry using multidetector digital pulse processing," *J. Vac. Sci. Technol. A* **36**, 02D407 (2018).
14. The Center for X-Ray Optics at Lawrence Berkeley National Laboratory, http://henke.lbl.gov/optical_constants.
15. S.-C. Lee, "Dependent scattering of an obliquely incident plane wave by a collection of parallel cylinders," *J. Appl. Phys.* **68**(10), 4952 (1990).
16. J. Schaefer, 2012, http://www.mathworks.com/matlabcentral/fileexchange/36831-matscat.
17. A. Kaskela et al., "Highly individual SWCNTs for high performance thin film electronics," *Carbon* **103**, 228–234 (2016).
18. D. L. Goldfarb, M. O. Bloomfield, and M. Colburn, "Thermomechanical behavior of EUV pellicle under dynamic exposure conditions," *Proc. SPIE* **9776**, 977621 (2016).
19. I. Pollentier et al., "Novel membrane solutions for the EUV pellicle: better or not?" *Proc. SPIE* **10143**, 101430L (2017).
20. P. J. van Zwol et al., "Emissivity of freestanding membranes with thin metal coatings," *J. Appl. Phys.* **118**, 213107 (2015).
21. P. J. van Zwol et al., "Pellicle films supporting the ramp to HVM with EUV," *Proc. SPIE* **10451**, 104510O (2017).
22. J. Beckers et al., "EUV-induced plasma: a peculiar phenomenon of a modern lithographic technology," *Appl. Sci.* **9**(14), 2827 (2019).
23. E. M. Malykhin et al., "Plasma cleaning of multilayer mirrors in EUV lithography from amorphous carbon contaminations," *Moscow Univ. Phys. Bull.* **66**(2), 184–189 (2011).
24. M. van de Kerkhof et al., "Particulate and molecular contamination control in EUV-induced H_2-plasma in EUV lithographic scanner," *Proc. SPIE* **11489**, 114890K (2020).
25. T. H. M. Van De Ven et al., "Ion energy distributions in highly transient EUV induced plasma in hydrogen," *J. Appl. Phys.* **123**(6), 063301 (2018).
26. A. Dolgov et al., "Comparison of H_2 and He carbon cleaning mechanisms in extreme ultraviolet induced and surface wave discharge plasmas," *J. Phys. D Appl. Phys.* **47**(6), 065205 (2014).
27. M. Y. Timmermans et al., "CNT EUV pellicle: moving towards a full-size solution," *Proc. SPIE* **10451**, 104510P (2017).
28. M. S. Dresselhaus et al., "Raman spectroscopy of carbon nanotubes," *Phys. Rep.* **409**(2), 47–99 (2005).
29. A. C. Dillon, M. Yudasaka, and M. S. Dresselhaus, "Employing Raman spectroscopy to qualitatively evaluate the purity of carbon single-wall nanotube materials," *J. Nanosci. Nanotechnol.* **4**(7), 691–703 (2004).
30. G. Zhang et al., "Hydrogenation and hydrocarbonation and etching of single-walled carbon nanotubes," *J. Am. Chem. Soc.* **128**(18), 6026–6027 (2006).
31. C. Laubis et al., "Update on EUV radiometry at PTB," *Proc. SPIE* **9776**, 977627 (2016).
32. N. Souza et al., "*In situ* tracking of defect healing and purification of single-wall carbon nanotubes with laser radiation by time-resolved Raman spectroscopy," *RSC Adv.* **5**(76), 62149–62159 (2015).
33. K. E. Hurst et al., "Cleaning of carbon nanotubes near the π-plasmon resonance," *Chem. Phys. Lett.* **433**(4–6), 301–304 (2007).
34. A. Suri and K. S. Coleman, "The superiority of air oxidation over liquid-phase oxidative treatment in the purification of carbon nanotubes," *Carbon* **49**(9), 3031–3038 (2011).
35. K. Ramadurai et al., "Raman and electron microscopy analysis of carbon nanotubes exposed to high power laser irradiance," *J. Appl. Phys.* **105**, 093106 (2009).
36. F. J. Ferrer et al., "Simultaneous quantification of light elements in thin films deposited on Si substrates using proton EBS (elastic backscattering spectroscopy)," *Nucl. Instrum. Methods Phys. Res. Sect. B* **332**, 449–453 (2014).
37. A. V. Talyzin et al., "Hydrogenation, purification, and unzipping of carbon nanotubes by reaction with molecular hydrogen: road to graphane nanoribbons," *ACS Nano* **5**(6), 5132–5140 (2011).
38. A. V. Krasheninnikov et al., "Stability of carbon nanotubes under electron irradiation: role of tube diameter and chirality," *Phys. Rev. B* **72**(12), 125428 (2005).

39. B. C. Satishkumar et al., "Electron beam induced structural transformations of SWNTs and DWNTs grown on Si_3N_4/Si substrates," *J. Nanosci. Nanotechnol.* **6**(5), 1350–1356 (2006).
40. S. Gupta, R. J. Patel, and R. E. Giedd, "Electron beam-induced surface modification and nano-engineering of carbon nanotubes: single-walled and multi-walled," *J. Mater. Res.* **21**(12), 3109–3123 (2006).
41. F. Banhart, "Irradiation of carbon nanotubes with a focused electron beam in the electron microscope," *J. Mater. Sci.* **41**(14), 4505–4511 (2006).

Marina Y. Timmermans is a researcher at IMEC in Leuven, Belgium. She received her PhD in applied physics from Aalto University, Helsinki, Finland, in 2013, working with carbon nanomaterial synthesis and application for electronics. After her doctoral research, she has joined IMEC and continued to be actively involved in engineering and integration of nanomaterials in functional applications.

Ivan Pollentier joined IMEC in 1993 after receiving his PhD in physics engineering from the University of Gent, Belgium, where he became involved in lithography engineering and development of i-line, DUV, and 193 nm processes toward IMEC's device programs. Since 2007, he is involved in resist and process-related R&D in the field of EUV lithography.

Maxim Korytov specializes in transmission electron microscopy since 2007. In 2010, he received PhD in physics studying III-V group semiconductors by quantitative TEM. He worked in Leibniz Institute for Crystal Growth, IKZ, Berlin, Germany, and Center for the Development of Materials and Structural Studies (CEMES, Toulouse, France) before joining IMEC in 2017.

Thomas Nuytten received his PhD in physics from KU Leuven in 2009 and subsequently worked as a postdoctoral researcher in the field of semiconductor nanostructures and energy conversion systems. In 2013, he joined IMEC as a senior researcher where his main interests include spectroscopic and electrical characterization of next-generation semiconductor technologies.

Stefanie Sergeant is an R&D assistant working for the materials and component analysis group at IMEC. She joined IMEC in 2016, after obtaining her Bachelor of Applied Science in chemistry. As an R&D assistant, she is focusing on Raman spectroscopy and scanning probe microscopy.

Thierry Conard is a team leader and principal member of technical staff of the chemical surface analysis team in IMEC located in Leuven, Belgium. He received his PhD degree in physics from the University of Namur (Belgium) in 1994 on electron spectroscopy characterization of copper oxides. After a post-doc at Waseda University (Tokyo, Japan), he joined IMEC in 1996 where he has been working since on the characterization of materials using photoemission and ToF-SIMS.

Johan Meersschaut is responsible for the ion beam analysis (RBS, ERD) activities at IMEC. He obtained the degree of PhD in physics in 1998 from KU Leuven (Belgium) for the study of magnetic multilayers with nuclear methods.

Yide Zhang received his Bachelor of Science in optical information science and technology in Ocean University of China in 2015. He continued with his MSc degree at Karlsruhe Institute of Technology (Karlsruhe, Germany), as part of which he carried out an internship work at IMEC focusing on the ion beam analysis of CNT membranes. Further he joined the University of Strasbourg (Strasbourg, France) with his main interests in nonlinear optics.

Masoud Dialameh joined IMEC as a researcher in 2020. His research mainly involves improving the accuracy of material characterisation by means of ion beam analysis and atom probe tomography. He received a PhD in physics from KU Leuven (Leuven, Belgium) and a PhD in metrology (cotutelle) from Politecnico di Torino (Turin, Italy) in 2019.

Wilfried Alaerts started at IMEC in 1998 as a litho operator. After 10 years he became a member of the lithography development group as a process assistant and is also supporting the pellicle research activities at IMEC.

Ehsan Jazaeri is a senior process engineer at IMEC specializing in SEM characterization of materials. He completed his PhD degree in materials science and engineering at Monash University, Australia, in 2018, working on design and fabrication of carbon nanotube composite fibers for enhanced mechanical properties. He joined IMEC in 2019 working on SEM characterization of conventional and new materials used in device fabrication.

Valentina Spampinato is a research member of the metrology group at IMEC since 2015. She is a ToF-SIMS expert. She received her PhD in materials science in 2012 from the University of Catania in Italy.

Alexis Franquet is leading the compositional analysis team of IMEC focusing on MS- and ToF-SIMS. He joined IMEC in 2005 as a researcher in surface analysis focusing on ToF-SIMS, AES and XPS. He received his PhD degree in applied physics from the University of Brussels (Belgium) in 2002.

Steven Brems is a team leader of IMEC's bonding, thinning and assembly 2D team. His PhD degree in physics was obtained at the KU Leuven in 2007 and was funded by the research foundation Flanders (FWO). In 2008, he started at IMEC and was involved in several research activities: chemical/mechanical cleaning, contamination control, growth and transfer of graphene and MX2 materials.

Cedric Huyghebaert is a program manager of exploratory processes and modules at IMEC, dealing with material exploration and early module integration for functional applications. He received his PhD in physics in 2006 at KU Leuven, Belgium. In 2005 he joined IMEC's pilot line as a support integration engineer, dealing with the process contamination control. He was part of the packaging group from 2007 to 2010, working as a senior integration engineer dealing with 3D-stacked IC integration. From 2010 to 2019 he led the nano-applications and material engineering group at IMEC.

Emily E. Gallagher is a principal member of technical staff at IMEC, focusing on pellicle membrane development, EUV imaging, and photomasks. She received her PhD in physics studying free electron lasers before shifting to semiconductors. She worked at IBM, most recently leading the EUV mask development effort, before joining IMEC in 2014.